Available online at www.sciencedirect.com
SCIENCE DIRECT
Remote Sensing of Environment 100 (2006) 441 – 456
Remote Sensing of Environment
www.elsevier.com/locate/rse

Estimation and vicarious validation of urban vegetation abundance by spectral mixture analysis

Christopher Small [a,*], Jacqueline W.T. Lu [b]

[a] *Lamont Doherty Earth Observatory, Columbia University, Palisades, NY 10964, USA*
[b] *City of New York Parks and Recreation, Central Forestry and Horticulture, Olmsted Center, Flushing Meadow Corona Park, Flushing, NY 11368, USA*

Received 31 May 2005; received in revised form 18 October 2005; accepted 20 October 2005

Abstract

Both moderate and high spatial resolution imagery can be used to quantify abundance and distribution of urban vegetation for urban landscape management and to provide inputs to physical process models. Estimation of vegetation fraction from Landsat ETM+ and Quickbird allows for operational monitoring and reconnaissance at moderate resolution with calibration and vicarious validation at higher resolution. Establishing a linear correspondence between ETM-derived vegetation fraction and Quickbird-derived vegetation fraction facilitates the validation task by extending the spatial scale from 30×30 m to a more manageable 2.8×2.8 m. A comparative analysis indicates that urban reflectance can be accurately represented with a three component linear mixture model for both Landsat ETM+ and Quickbird imagery in the New York metro area. The strong linearity of the Substrate Vegetation Dark surface (SVD) mixture model provides consistent estimates of illuminated vegetation fraction that can be used to constrain physical process models that require biophysical inputs related to vegetation abundance. When Quickbird-derived 2.8 m estimates of vegetation fraction are integrated to 30 m scales and coregistered to Landsat-derived 30 m estimates, median estimates agree with the integrated fractions to within 5% for fractions >0.2. The resulting Quickbird-ETM+ scatter distribution cannot be explained with estimate error alone but is consistent with a 3% to 6% estimation error combined with a 17 m subpixel registration ambiguity. The 3D endmember fraction space obtained from ETM+ imagery forms a ternary distribution of reflectance properties corresponding to distinct biophysical surface types. The SVD model is a reflectance analog to Ridd's V–I–S land cover model but acknowledges the fact that permeable and impermeable surfaces cannot generally be distinguished on the basis of broadband reflectance alone. We therefore propose that vegetation fraction be used as a proxy for permeable surface distribution to avoid the common erroneous assumption that all nonvegetated surfaces along the gray axis are completely impermeable. Comparison of mean vegetation fractions to street tree counts in New York City shows a consistent relationship between minimum fraction and tree count. However, moderate and high resolution areal estimates of vegetation fraction provide complementary information because they image all illuminated vegetation, including that not counted by the in situ street tree inventory.

Keywords: Urban; Vegetation; Landsat; Quickbird; Spectral mixture analysis; Calibration: validation

1. Introduction

Vegetation abundance and distribution are primary determinants of urban environmental conditions. In addition to its obvious aesthetic importance, vegetation exerts a strong influence on mass and energy fluxes through the urban environment by modulating evapotranspiration and absorption of solar radiation. Accurate mapping and monitoring of vegetation distribution and condition is also central to the understanding of urban ecosystems, including its role in mitigating air pollution and reducing the urban heat island effect. Resource managers can also use information on the abundance, condition and spatial distribution of urban vegetation for park and natural area management and urban planning. While in situ data collection is the primary means of measuring and monitoring urban vegetation, remotely sensed observations can provide valuable complements to traditional field observations. Accurate, detailed maps of urban vegetation also have application in regional scale models of climatic, hydrologic and ecologic processes.

* Corresponding author.
E-mail addresses: small@LDEO.columbia.edu (C. Small), Jacqueline.Lu@parks.nyc.gov (J.W.T. Lu).

0034-4257/$ - see front matter © 2005 Published by Elsevier Inc.
doi:10.1016/j.rse.2005.10.023

New York City, most famous for its skyscrapers and worldly population, is also home to an estimated 5.2 million trees (Nowak & Crane, 2002). New York City's vegetation is comprised of a patchwork of remnant forests, inherited estates, neighborhood parks and playgrounds, green streetscapes, parkways and private backyards and roof gardens. New York City Parks and Recreation (Parks) has jurisdiction for over half of the estimated 5 million total trees in the city. From 1995 to 1996, Parks mobilized over 700 volunteers to conduct a comprehensive census of all the street trees in New York City. The census counted over 498,000 street trees in New York City, consisting of approximately 70 different varieties. The vast majority of trees, however, are comprised of a small number of species; over 40% of the street tree population consists of just two species, Norway maple (*Acer platanoides*) and London plane tree (*Platanus acerifolia*). New York City's street trees are relatively small, with almost 60% measuring less than 12 in. diameter at breast height (Watt, 1998). However, many other types of vegetation in New York City, managed or impacted by Parks and at least another dozen city, state, and federal agencies and private actors, are not well characterized through on the ground inventories. Management of New York's trees by Parks relies on the street tree census to represent the spatial distribution and health of its vegetative assets. Remotely sensed quantitative estimates of urban vegetation abundance and distribution could potentially provide a valuable complement to tree inventories and in situ monitoring. However, the operational use of remotely sensed estimates requires a robust estimation methodology and a well-defined validation procedure to determine the accuracy of the estimates.

A primary requirement for operational use of remotely sensed vegetation abundance estimates is that they provide physical units that can be compared directly with other measures of vegetation abundance and condition. Spectral Mixture Analysis (SMA) satisfies this requirement by providing pixel-scale estimates of areal abundance of spectral endmembers (Adams et al., 1986; Smith et al., 1990). In recent years SMA has been used for a variety of urban land cover mapping applications (e.g. Kressler & Steinnocher, 1996; Small, 2001a; Small & Miller, 1999; Rashed et al., 2001, 2002; Wu & Murray, 2003; Weng et al., 2004). In comparison to vegetation indices (e.g. Normalized Difference Vegetation Index (NDVI)), SMA offers the advantage of providing estimates of areal vegetation abundance that can be compared directly to other measures of vegetation cover per unit area. The SMA methodology has been rigorously defined (Adams et al., 1986; Gillespie et al., 1990; Sabol et al., 1992; Settle & Drake, 1993; Smith et al., 1990) and has been shown to be sufficiently stable for multitemporal change analyses (Adams et al., 1995; Elmore et al., 2000; Small, 2002b). In spite of its increasingly widespread use, most spectral mixture analyses do not validate the endmember fraction estimates they produce. Elmore et al. (2000) devised a rigorous field validation methodology based on point frame transect measurement of individual plants in a semiarid environment but the procedure is very labor intensive and not suitable for environments containing large trees. Small (2001a) proposed a methodology for high spatial resolution vegetation abundance validation from aerial photographs but the procedure relies on manual selection of specific validation sites and is also somewhat labor intensive. In light of the current availability of calibrated high (<5 m) resolution multispectral imagery from Ikonos and Quickbird, the potential for quantitative validation of fractional abundance estimates has increased considerably since the time these earlier studies were conducted. High spatial resolution imagery also provides a means to examine the structural characteristics of moderate resolution (~20–40 m) targets as well.

The objectives of this study are to provide operational procedures for moderate resolution vegetation fraction estimation and validation and to examine some of the factors that limit the use of vegetation fraction estimates for urban applications. Rigorous calibration and validation of image-derived quantities generally requires direct field measurements of the variable being estimated. However, establishing a linear correspondence between ETM-derived vegetation fraction and Quickbird-derived vegetation fraction can facilitate the validation task by extending the spatial scale from 30×30 m to a more manageable 2.8×2.8 m. Since vegetation fraction is much easier to validate at 2.8 than 30 m scales, we refer to this process as vicarious validation. In the first part of the analysis we summarize the procedure used to derive vegetation fraction estimates from Landsat and Quickbird imagery. The theoretical basis and stability of the procedure used here are explained in greater detail in Small (2001a) and Small (2003) as well as many earlier works cited therein. Here we provide a summary of the procedure with emphasis on how it can be made operational. In the second part of the analysis we quantify the agreement between the moderate and high resolution estimates and investigate the effects of estimate error and spatial misregistration. The discussion focuses on the physical interpretation of vegetation fraction estimates and comparison to in situ measures of urban vegetation abundance. The results of the analysis highlight factors affecting vicarious validation of Landsat mixture fractions with Quickbird fractions and provide quantitative estimates of the magnitude of different sources of error in the process.

2. Data

In this study we derive moderate resolution estimates of aggregate vegetation fraction from Landsat imagery and quantify the correspondence between these estimates and integrated vegetation fraction measurements derived from high resolution Quickbird imagery (Fig. 1). Both images used in this study were acquired in August 2002. At the time, the New York metro area was experiencing drought conditions following several years of below average precipitation. Although some smaller trees were experiencing premature senescence by August, the vegetation abundance within the study area was equivalent to full leaf-on conditions at the time that both images were acquired. We do not believe that the vegetation cover changed significantly between the times the images were acquired. The Landsat ETM+ image (p. 14, r. 32) used in this

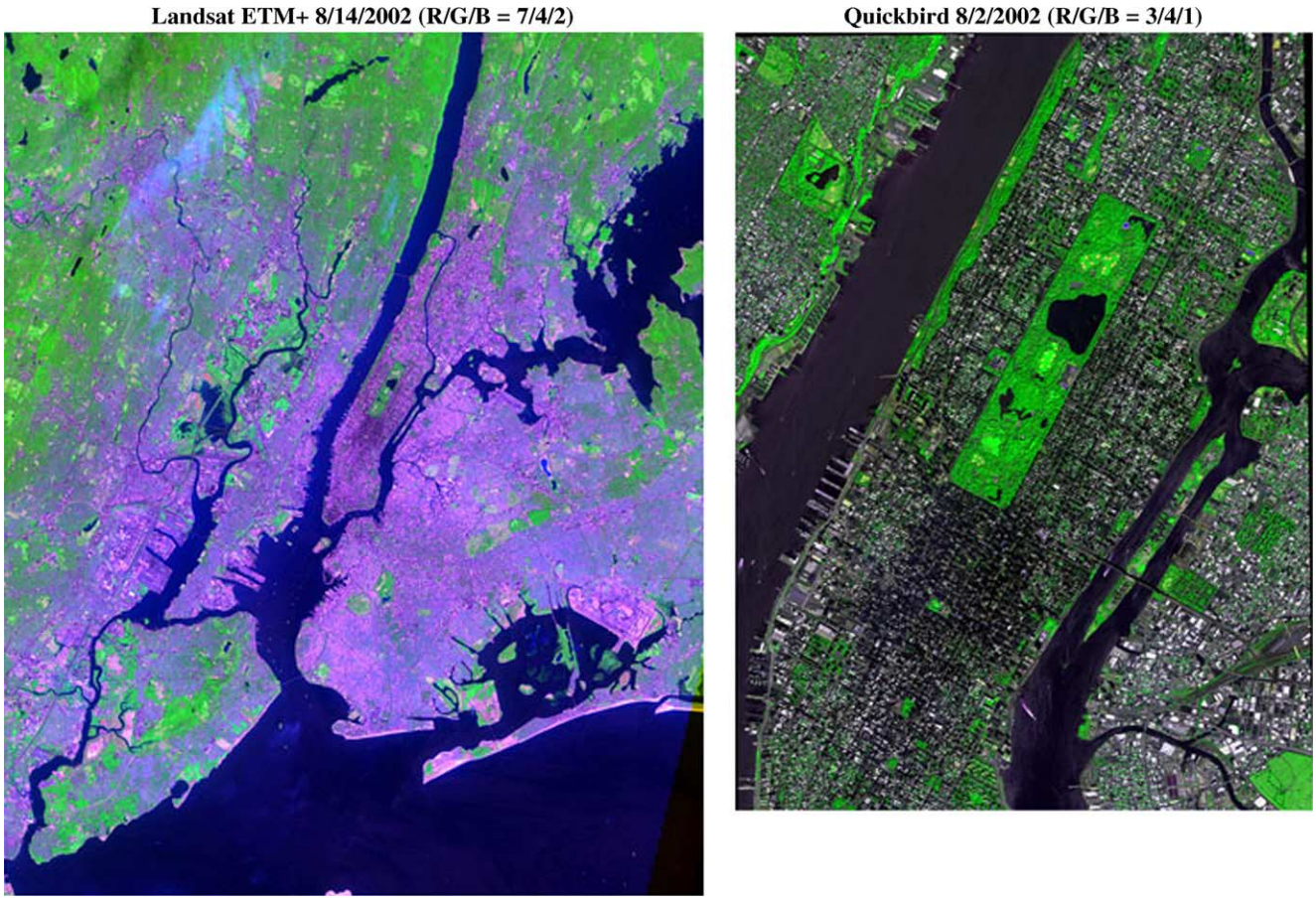

Fig. 1. False color imagery of the New York metro area in August 2002.

study was acquired on 14 August 2002 at ~9:30 EDT. Image DNs were converted to exoatmospheric reflectance units as described by Markham and Barker (1986, 1987) and in the Landsat 7 Users Handbook (http://ltpwww.gsfc.nasa.gov/IAS/handbook/handbook_toc.html). No atmospheric correction was applied. The Quickbird imagery was acquired on 2 August 2002 at 09:48 EDT from an elevation angle of 79.5° with a solar elevation of 68°. Image DNs were converted to at-sensor radiance using parameters provided by Digital Globe. Spatial accuracy of the georegistered images were verified to be within 31 m by comparison with 48 validation sites derived from a 2001 Garmin 12 Map handheld GPS receiver. Coregistration accuracy of the two images is discussed in detail below.

3. Spectral mixture analysis and endmember selection

Spectral Mixture Analysis (SMA) is a methodology whereby an observed radiance is modeled as a linear mixture of spectrally pure endmember radiances. Linear mixture models are based on the observation that, in many situations, radiances reflected from surfaces with different "endmember" reflectances mix linearly in proportion to the area of each endmember within the Instantaneous Field Of View (IFOV) (Johnson et al., 1983; Singer, 1981; Singer & McCord, 1979). This observation has made possible the development of a systematic methodology for spectral mixture analysis (Adams et al., 1993, 1986; Gillespie et al., 1990; Sabol et al., 1992; Smith et al., 1990) in which land surface reflectance variations are described by a set of endmember fraction images representing spatial variations in the areal abundance of each endmember. Although the physical process represented by the mixture model corresponds to the measurement of a mixed radiance within the sensor IFOV, the model can also be applied to exoatmospheric reflectances because the conversion equations are linear. If a limited number of spectrally distinct endmembers can be found it is possible to define a mixing space within which mixed pixel spectra can be described as linear mixtures of the endmember spectra. A mixing space is analogous to a spectral feature space but is generally represented with low dimensional projections of the principal components (PCs) of the image rather than the observed radiance bands. Representing a multispectral feature space with the low order PCs allows the topology of the space to render as a 3D construct. With Landsat imagery, the three primary PCs generally contain more than 95% of the variance in the image (Small, 2004).

Given sufficient spectral resolution, a system of linear mixing equations and endmembers can be defined and the best fitting combination of endmember fractions can be estimated for each of the observed reflectance spectra. The solution to the linear mixing problem can be cast as a linear inverse problem in which the system of mixing equations is inverted to yield

estimates of the endmember fractions that best fit the observed mixed reflectances (Boardman, 1993; Boardman & Kruse, 1994; Settle & Drake, 1993). It is important to note that even when the surface within the Ground Instantaneous Field Of View (GIFOV) is not a mixture of the unique, spectrally pure endmember materials, it can be *represented* as such a mixture if it lies within the bounds of the mixing space. Because the methodology provides a general physical representation of mixed reflectances, it has proven successful for a wide variety of quantitative applications with multispectral imagery (e.g. Adams et al., 1993, 1986; Elmore et al., 2000; Pech et al., 1986; Roberts et al., 1998a; Smith et al., 1990).

The feasibility of the linear mixture model depends on the topology of the spectral mixing space in which the observed spectra reside. The mixing space is the N dimensional cloud of image pixels corresponding to all of the image spectra to be represented by the mixture model. The mixing space can be represented graphically as scatterplots of the various band combinations corresponding to different 2D projections of the N dimensional cloud. The dimensionality of the problem can be reduced by focusing on the dimensions of the mixing space that contain the majority of the image variance. A principal component transformation can be used to reorient (rotate) the mixing space and provide quantitative estimates of the variance accounted for by each principal component (PC). Principal component analyses of Landsat and Ikonos imagery indicate that >90% of image variance can generally be represented with the three primary PCs of the mixing space (Small, 2001b). This allows us to represent the topology of the mixing space with three orthogonal projections of the 3D pixel cloud formed by the three primary PCs. The mixing space of the NYC ETM+ imagery is shown in Fig. 2. In this case, the triangular topology of the mixing space suggests that the mixed reflectances contained within can be represented by a three endmember mixing model. The apexes of the 3D mixing space correspond to the spectral endmembers while the mixed pixel reflectances lie within a convex hull circumscribing the apexes (Boardman, 1993). The reflectance vectors residing at the three apexes of the NYC ETM+ mixing space are shown in Fig. 2d. These endmember spectra correspond to High Albedo Substrate, Vegetation and Dark surfaces. The triangular topology of the NYC ETM+ mixing space is very similar to that of other urban areas worldwide (Small, 2002a, 2005) as well as the global ETM+ mixing space (Small, 2004). The straight edges

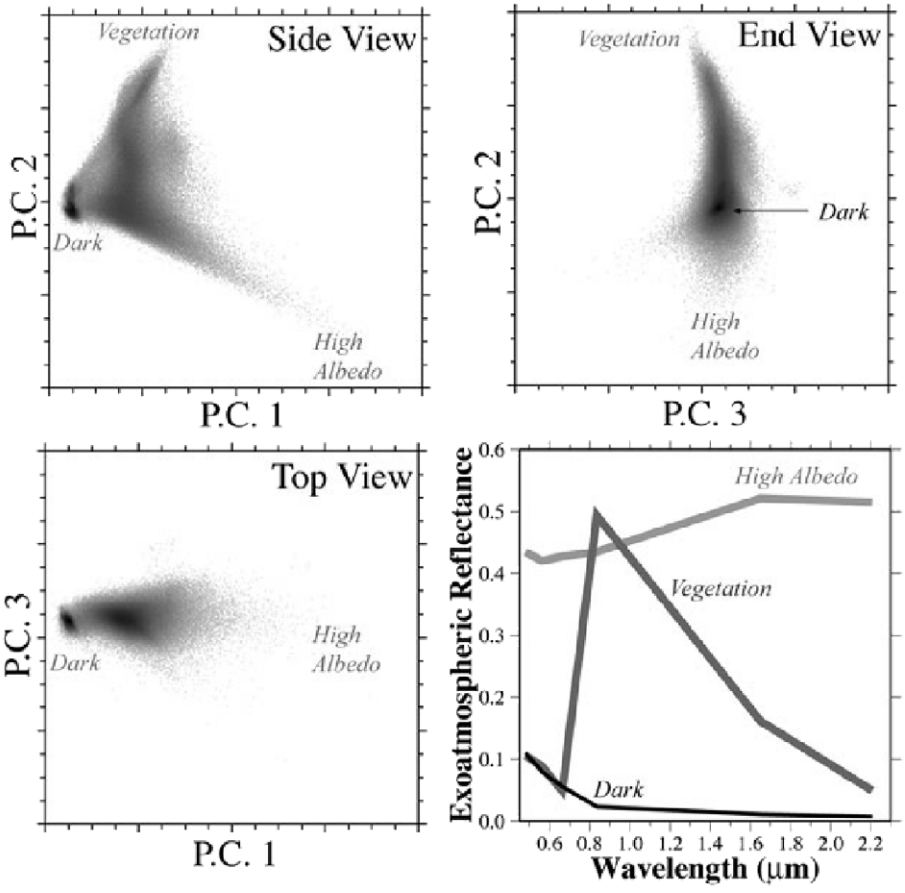

Fig. 2. Spectral mixing space and endmembers for the NYC ETM+ image. Density shaded scatterplots show the distribution of pixels within the spectral mixing space defined by the first three principal components containing >95% of the image variance. The side view shows a triangular mixing space bounded by high albedo, vegetation and dark surface endmembers at the apexes. The top and end views show the third dimension of the mixing space indicating that it is primarily planar along the mixing continuum extending to the vegetation endmember. Most of the nonlinearity is associated with the gray axis spanning the other two endmembers. Endmember spectra are associated with highly reflective surfaces (e.g. warehouse roofs), clear deep water (Central Park Reservoir) and large manicured grass areas (Central Park Great Lawn).

extending from the Dark surface endmember indicate that binary mixing between the Dark and Vegetation endmembers is strongly linear (Fig. 2a). The mixing continuum between the Dark and High Albedo endmembers also appears to be linear in the side view (Fig. 2a) but the end view of the mixing space reveals convexity in the third dimension suggesting a small degree of nonlinear mixing along this "gray axis" (Fig. 2b). The concave edge of the mixing space between the Vegetation and High Albedo Substrate endmembers is consistent with the linear model although the concavity suggests that mixtures of these two endmembers always contain some amount of the Dark endmember also (Fig. 2a). Pure binary mixtures of the vegetation and substrate endmembers would fall along a straight line between these apexes of the mixing space.

The selection of appropriate spectral endmembers is essential to the accuracy of the mixture model. The sensitivity of fraction estimates to endmember variability in broadband mixing spaces is not as great as in hyperspectral mixing spaces but it can have a significant impact on the accuracy of the results. The methodology described here relies on manual selection of endmember spectra from the apexes of the mixing space. This is feasible for vegetation fraction estimation because broadband mixing spaces invariably taper approaching the vegetation endmember. Analyses of a wide variety of Landsat and Ikonos mixing spaces consistently show well defined vegetation apexes with little variability (Small, 2003, 2004, 2005). The same is generally true of the dark surface endmember, although sometimes to a lesser extent if multiple spectrally distinct water bodies, shadows and absorptive surfaces are present in the scene. Selection of the high albedo substrate endmember presents the greatest challenge because of the frequently divergent topology of broadband mixing spaces in the vicinity of high albedo endmembers. Fortunately, vegetation fractions are relatively insensitive to moderate variability at high fractions of the high albedo substrate endmember because purely binary mixing between vegetation and high albedo substrate is extremely rare (Small, 2004). The ubiquitous presence of shadow in partially vegetated landscapes generally results in ternary mixing between the vegetation, substrate and shadow. The approach used here selects the most extreme (i.e. distant from the dark surface apex of the mixing space) high albedo substrate spectrum that lies closest to the linear trend of the gray axis spanning the dark surface and high albedo substrate endmember. The same approach is used to select the vegetation endmember, although it is less critical because the mixing space tapers approaching the vegetation apex resulting in negligible

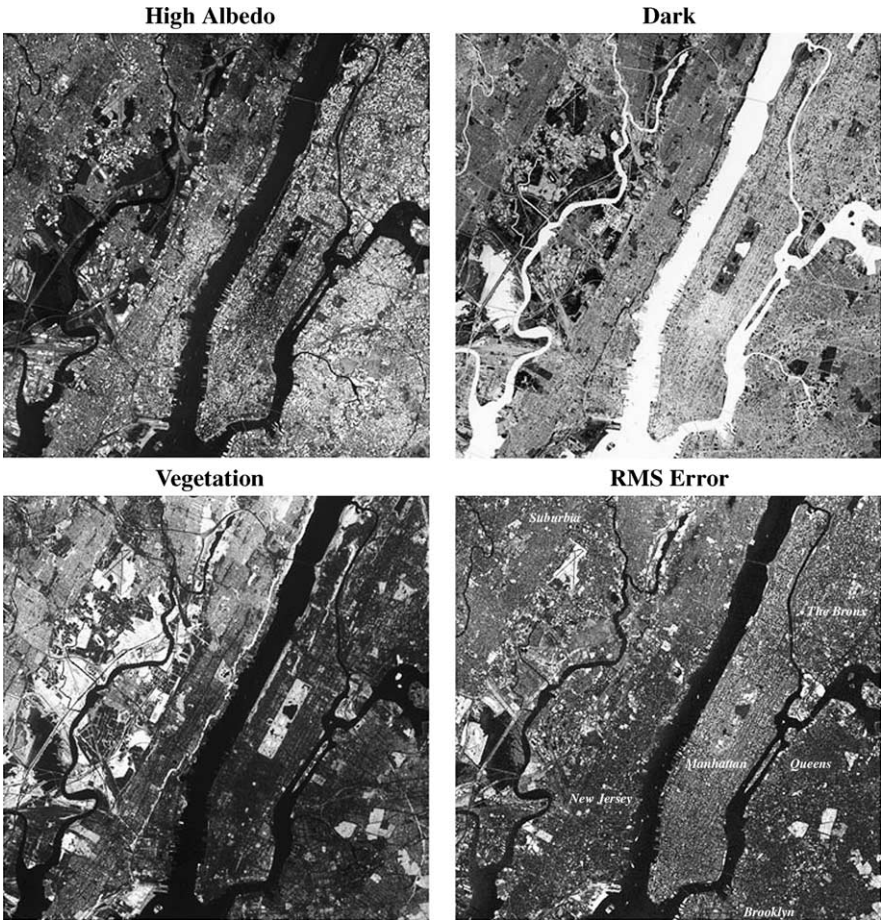

Fig. 3. Endmember fractions and RMS error for the ETM+ three endmember linear mixture model for the New York metro area. Higher fractions (and error) are indicated by lighter shading. A 2% linear stretch has been applied to each image. Histograms of each fraction are given in Fig. 4. Spatially contiguous areas of higher RMS error (0.03 to 0.06) correspond to partially exposed soil that is not represented by the three endmember model. Note the neighborhood scale variations in vegetation abundance.

variability of the vegetation endmember. The advantage of manually selecting the endmember spectra from the mixing space is that it provides an opportunity to determine the inherent variability in the spectra near the apex of the mixing space. High dimensional hyperspectral imagery generally requires numerical and statistical approaches to endmember selection (e.g. Asner, 1998; Asner and Lobell, 2000; Roberts et al., 1998b) but the low dimensionality of multispectral imagery allows the analyst to mitigate endmember variability directly by selecting the endmembers that are consistent with the binary mixing continua among endmembers while avoiding the spurious spectra that often reside near the apexes of the mixing space.

Endmember fractions are estimated with a constrained least squares inversion following the procedure described in detail by Small (2001a). The resulting fraction and RMS error distributions–shown in Figs. 3 and 4–are very similar to those obtained by Small (2001a, 2001b). This is expected given the similarity in the study area and endmember spectra. The RMS error image shows land cover types that are not well represented in the model. As in the previous study, the largest misfits are associated with areas of exposed soil and isolated high albedo targets that are spectrally distinct from the high albedo substrate endmember. This is consistent with the lack of a second substrate endmember in the model and the fact that the mixing space diverges approaching the single high albedo substrate endmember (as seen in Fig. 2c). Fig. 4 shows RMS error diminishing with increasing fractions of Dark and Vegetation endmembers. This indicates that the inverse problem is well posed with respect to vegetation fraction estimation. RMS error is generally less than 0.03 reflectance units, suggesting that the 3 endmember linear model is capable of replicating the observed mixed reflectances quite closely. This does not, however, guarantee that the fraction estimates are accurate. The accuracy must be determined through validation.

4. Vicarious validation and calibration

We attempt to validate the ETM+ vegetation fraction estimates by quantifying their degree of correspondence to vegetation fraction estimates derived from Quickbird multispectral imagery. For estimates of areal vegetation abundance, the 2.8 m spatial resolution of the Quickbird sensor allows it to image the individual components of the urban mosaic at significantly higher spatial resolution than the 20 to 30 m characteristic scale estimated for the New York urban mosaic (Small, 2003). This is why individual features like buildings, sidewalks, streets and trees can be identified in Quickbird imagery. The 2.8 m resolution is more than adequate to image

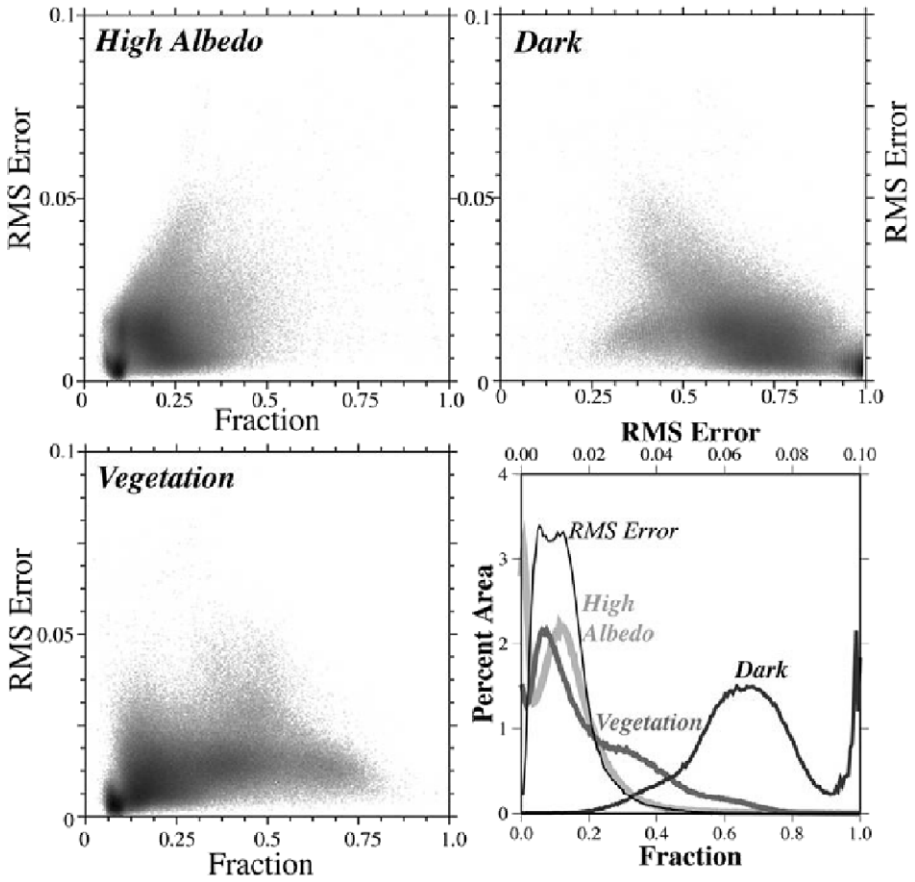

Fig. 4. RMS error and endmember fraction distributions for the ETM+ linear mixture model. Density shaded scatterplots show diminishing error for increasing fractions of dark and vegetation endmembers indicating that the linear model is well posed for these endmembers. RMS error increases for increasing fractions of the high albedo endmember because a single high albedo endmember does not represent all of these reflectances accurately. Histograms show the dominance of dark fractions and the generally low (<0.03) RMS error for the NYC ETM+ image.

medium to large tree crowns and to detect the presence of fairly small street trees. For the size distribution of trees in the study area, the Quickbird sensor is able to image all components of the urban vegetation that make a significant contribution to the mosaic imaged by the ETM+ sensor. At the scale of the ETM+ GIFOV, each 2.8 m Quickbird pixel represents less than 1% of the area within the 30 m Full Width Half Max of the ETM+ point spread function. This is more than adequate to represent the spatial scale of the dominant targets responsible for the multiple scattering that is the primary source of nonlinear mixing within the ETM+ GIFOV. Because nonlinear mixing is the primary source of error in this estimation problem, we consider the spatial oversampling provided by the Quickbird data to be well suited to address the fundamental question in the mixing problem. The question is whether inversion of the linear mixing model yields areal vegetation estimates that are consistent with actual measurements of vegetated area. Quickbird easily resolves the smallest individual vegetated components of the urban mosaic so the sum of the 2.8 m vegetation fractions within the ETM+ GIFOV gives a measure of the vegetated area of each pixel.

The validity of using high resolution vegetation fractions to validate moderate resolution fractions therefore depends on whether there is a consistent bias in the linear mixing model that corrupts both the moderate and high resolution estimates in such a way that they are mutually consistent but consistently wrong. This suggests a telescoping calibration/validation strategy that could be extended to sub-meter scales with direct field measurements. For mature deciduous trees like those in New York, this would require a separate experiment that is beyond the scope of the present analysis. For the purposes of this study, we will consider the degree of correspondence between the ETM+ and Quickbird vegetation fractions to be an adequate metric for the accuracy of the ETM+ vegetation fractions. Because the mixing problem is well posed for Quickbird and because we have field validated the Quickbird fractions in Manhattan we will refer to the integrated Quickbird vegetation fractions as measurements at 30 m scales. We feel this is justified because the Quickbird resolves all areally significant components of urban vegetation at 2.8 m resolution and the integrated fraction is the total measure of the more spatially detailed vegetation distribution.

The characteristics of the Quickbird mixing space are similar to the ETM+ mixing space described above and almost identical to those of the Ikonos MSI mixing space described in detail by Small (2003). The Quickbird mixing space and spectral endmembers for the NYC study area are shown in Fig. 5. The Quickbird mixing space is similar to the ETM+ mixing

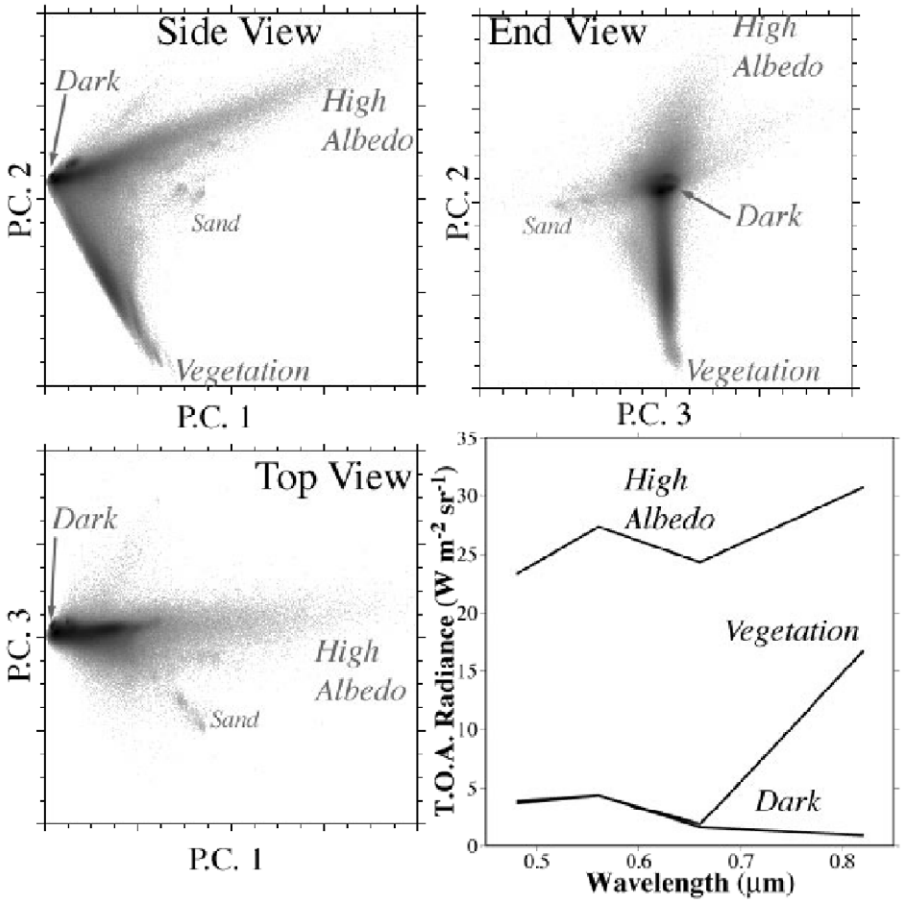

Fig. 5. Spectral mixing space and endmembers for the NYC Quickbird image. The side view shows the familiar triangular mixing space with high albedo, vegetation and dark surface endmembers. The top and end views show the third dimension of the mixing space indicating that it is primarily planar along the mixing continuum extending to the vegetation endmember and that most of the nonlinearity is associated with the gray axis spanning the other two endmembers. Sand ballfields are spectrally distinct.

space in both dimensionality, linearity and endmembers. The most obvious difference is the greater dominance of binary mixing between the dark surface endmember and the other two. This is expected as the higher spatial resolution of the Quickbird imagery will result in less mixing between distinct components of the urban mosaic (streets, roofs, trees, etc.) but does not eliminate the finer scale shadowing from textural features and illumination differences that modulate the brightness of individual components of the mosaic. Differences in illumination and texture (resulting in internal shadowing) are manifested as binary mixtures between the dark surface and the other two endmembers. This is why high resolution mixing spaces are more concave and tend to resemble distinct binary mixing continua radiating outward from the dark surface endmember.

The procedure used to estimate vegetation fractions from the Quickbird imagery is analogous to that described above for the ETM+ imagery. Spectral endmembers are selected from the apexes of the mixing space and verified with field visits. The vegetation endmember corresponds to several patches of recently planted turf on the Great Lawn and well-maintained bowling greens in Central Park. We consider dense, healthy turf equivalent to a 100% vegetated surface with negligible shadow. Quickbird-derived vegetation fractions for the entire validation area and a full resolution subset are shown in Fig. 6. Note the variability within individual tree crowns and within the grass patches having higher vegetation fractions. These are consequences of internal shadowing within the crowns and spatial variations in the health and density of the grass cover. The unit sum constrained least squares inversion of the Quickbird data results in RMS misfits of less than 2% of red-edge amplitude for greater than 95% of image pixels. The red-edge amplitude is used as a metric here because it generally spans the range of reflectances observed in a vegetation spectrum. As in the ETM+ inversion, RMS error diminishes with increasing vegetation fraction. This is consistent with the strongly linear mixing and tapering of the mixing space approaching the vegetation endmember.

The ETM+ vegetation fraction estimates are validated by direct comparison to the Quickbird estimates. In order to compare the two vegetation fractions it is necessary to duplicate the sampling operation that occurs within the ETM+ sensor. We follow the procedure used by Small (2001a) in which the 2.8 m vegetation fractions are convolved with the point spread function (spatial response) of the ETM+ sensor and resampled at 30 m resolution. We use an axisymmetric 2D equivalent of the line spread function published by Markham (1985) approximated by a Gaussian kernel with a 30 m Full Width Half Max. The filtered and resampled 30 m vegetation fractions are shown alongside the ETM+ estimates in Fig. 7.

Convolution and resampling of the 2.8 m vegetation fractions at 30 m resolution makes it possible to assess the geographic coregistration and to compare the moderate resolution estimates and the high resolution measurements directly. Comparison of the Quickbird image to the handheld GPS measurements showed a generally northeastward displacement of 10 to 30 m. This is assumed to be the result of

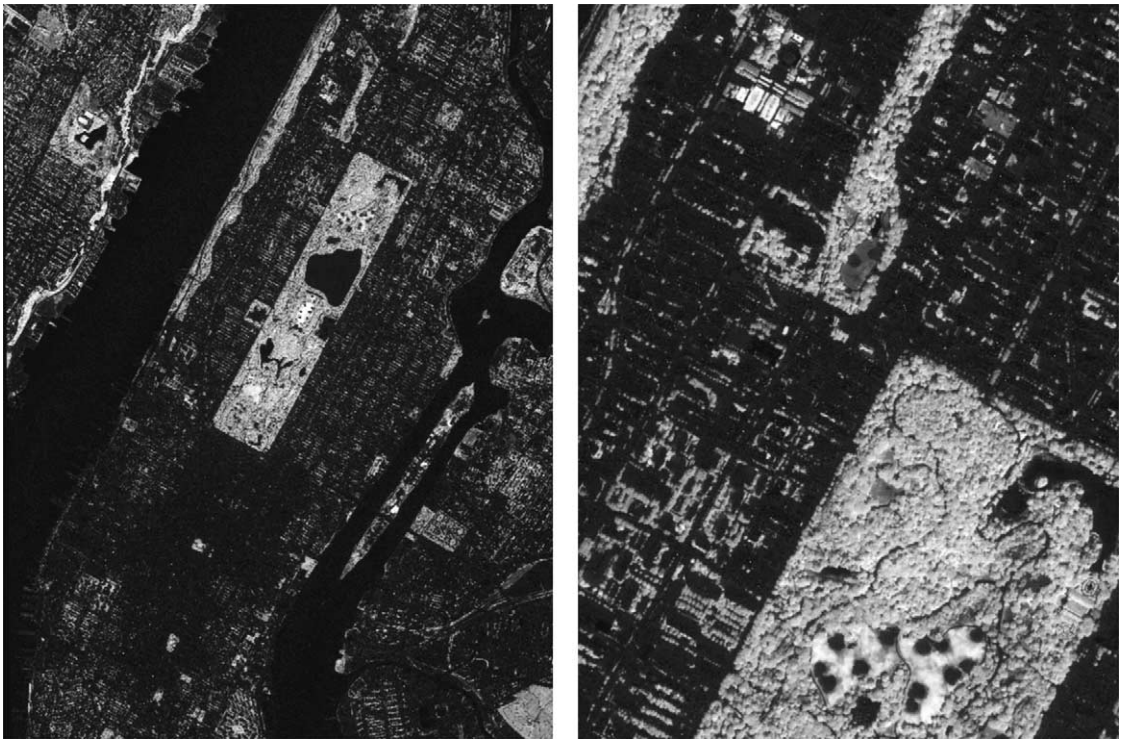

Fig. 6. Quickbird-derived vegetation fraction for central Manhattan and adjacent areas. The left image shows the entire scene ($\sim 7 \times 10$ km) at reduced resolution and the right image shows a 1.5×2 km subset at full resolution. Gray shading shows vegetation fraction between 0 and 0.7. Dense, well-maintained lawns in Central Park (near center of left image) are calibrated as 100% illuminated vegetation.

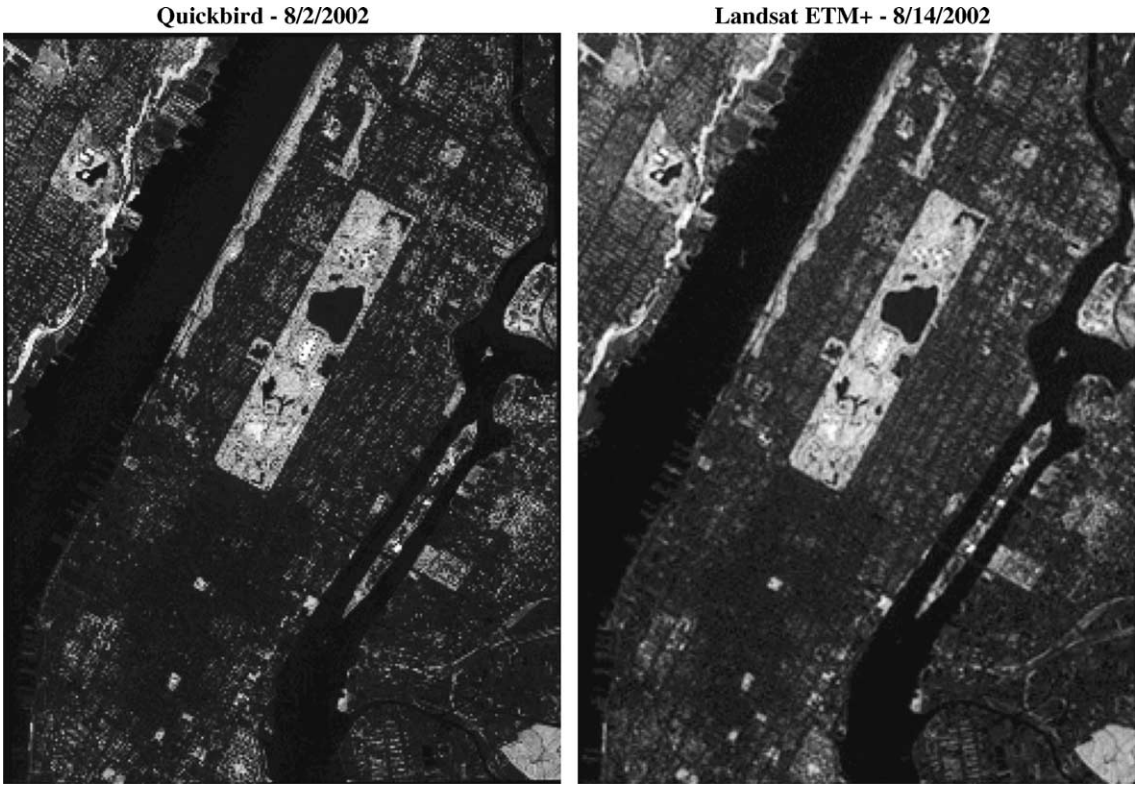

Fig. 7. Quickbird and Landsat ETM+ 30 m vegetation fraction estimates for central Manhattan and adjacent areas. The Quickbird fractions are derived from 2.8 m estimates convolved with the ETM+ point spread function and resampled at 30 m resolution. Gray shading shows vegetation fraction between 0 and 0.7. Both images were acquired under drought conditions.

error in the Quickbird geolocation and error in the GPS position estimate related to multipathing and limited satellite availability within the urban canyons. As this is within the spatial uncertainty of GPS receiver and the expected geolocation error of both images, we did not attempt to relocate either image. Visual comparison of the interactively overlaid 30 m images showed no evidence for systematic misregistration. A density shaded scatterplot of the 30 m ETM+ estimates versus the 30 m resampled Quickbird vegetation fractions is shown in Fig. 8. The linear correlation coefficient for the 80,850 (245×330) coregistered 30 m pixels is 0.89. Medians and interquartile ranges calculated at 1% increments indicate that the ETM+ estimates agree with the Quickbird vegetation fractions to within 5% for fractions greater than 0.2 and that 50% of ETM+ fractions agree to within 10%. The ETM+ fractions are consistently higher than the Quickbird estimates for fractions less than 0.2 with the positive bias diminishing monotonically approaching 0.2. One possible cause for the consistent positive bias at fractions <0.2 could be the spatial nonuniformity of the ETM+ point spread function. Scatter about the 1:1 line increases for fractions up to ~0.3 and diminishes for higher fractions.

4.1. Error modeling

We investigate two possible causes for this scatter by simulating the effects of spatial misregistration and systematic estimation error. The scatter about the 1:1 line could result from (1) error in the ETM+ and Quickbird fraction estimates or from (2) subpixel (<30 m) spatial misregistration between the ETM+ and Quickbird images or from (3) a combination of estimate error and spatial misregistration. Spatial misregistration of any pair of images causes the spatial correlation between them to diminish as the scatter increases with offset between the images. It is not feasible to derive a simple analytic expression for the decorrelation because the nature of scatter that results from the spatial misregistration depends on the actual spatial distribution of the vegetation in the study area. The effect of spatial misregistration can however be simulated by introducing a series of geographic offsets to identical 2.8 m vegetation fraction images, convolving each image with the ETM+ spatial response function, resampling each to 30 m resolution and comparing the correlation of the displaced 30 m images. We simulated the effects of spatial misregistration for eastward, northward and northeastward offsets ranging from 2 to 50 m and compared the resulting scatterplots and linear correlation coefficients with those estimated for the ETM+ and resampled Quickbird vegetation fractions. Fig. 9 shows the progressive decorrelation of both the 2.8 m fractions and the resampled 30 m fractions for different distance and directional offsets. As expected, the correlation of the 2.8 m fraction images diminishes rapidly while the smoothing effect of the ETM+ response function reduces the effect of subpixel (<30 m) offsets by increasing the correlation between adjacent pixels. In both cases, the northeastward displacements decorrelate more rapidly than either the northward or eastward displacements

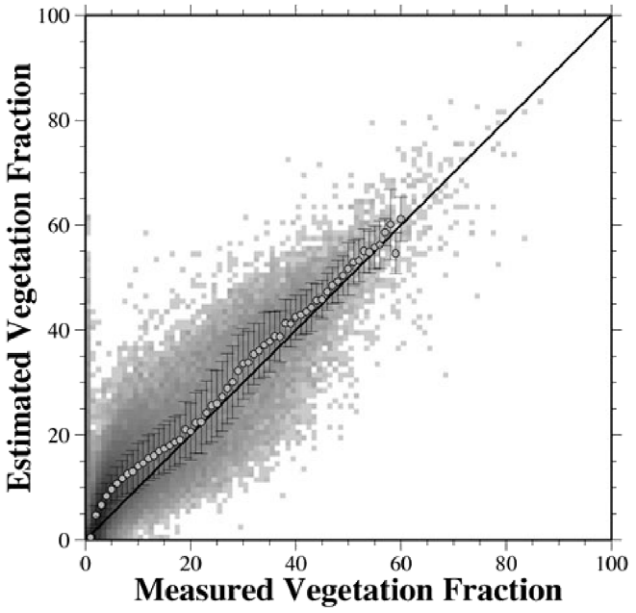

Fig. 8. Measured versus estimated vegetation fractions for the New York validation site. Measured fractions are calculated from 2.8 m Quickbird estimates integrated to 30 m. Estimated fractions are derived from Landsat ETM+ estimates coregistered to the resampled Quickbird image. Circles show median estimated fractions and bars show interquartile ranges in 1% bins. Darker pixels correspond to larger numbers of 30 m samples. Medians are within 5% for fractions greater than 0.2. The observed scatter about the 1:1 line may result from estimation error and/or subpixel image misregistration.

alone. Together, these simulations suggest that the observed correlation of 0.89 could be explained by image misregistrations of 16 to 24 m. However, it is unlikely that the scatter would be caused by spatial misregistration alone because some amount of estimation error must be expected. A more general error model incorporates both misregistration and estimation error.

We simulate the combined effects of spatial misregistration and estimation error by comparing scatterplots of perturbed versus unperturbed vegetation fractions. In general, we would expect some amount of subpixel spatial misregistration in both northward and eastward directions as well as some amount of error in the estimation of the ETM+ and Quickbird fractions. By varying the amount of misregistration and the amount of estimation error we can compare the dispersion of the resulting scatterplots with that observed in Fig. 8. The effect of geolocation error was simulated as described above. In addition, we simulated the effect of estimation error by adding specified amounts of normally distributed random noise to each pixel in the perturbed image. A correlation array of density shaded scatterplots for a range of spatial offsets and noise variances is shown in Fig. 10. It is immediately apparent that the observed tapered dispersion about the 1:1 line seen in Fig. 8 is different from the uniform dispersion resulting only from the addition of estimation error (column 4 in Fig. 10). The distribution of scatter in Fig. 8 is most similar to that seen for a northeastward misregistration of 17 m with less than 3% estimation error or an 11 m misregistration with less than 6% estimation error.

5. Discussion

5.1. Reflectance of pervious and impervious surfaces

The Substrate, Vegetation, Dark surface (SVD) reflectance model used in these spectral mixture analyses represents areal fractions of three biophysically distinct components of the urban land surface. Specifically, these are the fraction of illuminated vegetation, illuminated solid substrate and the fraction of shadowed and nonreflective surface of all types. The dark surface endmember can also represent transmissive surfaces like water. Because so little energy is returned from dark surfaces the radiance field conceals a fundamental ambiguity among transmissive surfaces (like clear water) and low albedo illuminated surfaces (like roofing tar) and shadowed surfaces of all kinds. However, water can generally be distinguished from shadow in the mixing space because of its homogeneity and clustering in the feature space. The primary ambiguity lies between illuminated low albedo surface and deeply shadowed surface. Nonetheless, the three endmember SVD reflectance model does represent the land surface as independent components of the biophysical landscape with decidedly different energetic, hydrologic and ecologic properties. The independence of the SVD fractions in the planar endmember fraction feature space (Fig. 11a) corresponds to a ternary abundance diagram when the mixing plane is viewed orthogonal to the mixing plane (Fig. 11d). This is conceptually similar to Ridd's Vegetation–Impervious–Soil (VIS) ternary

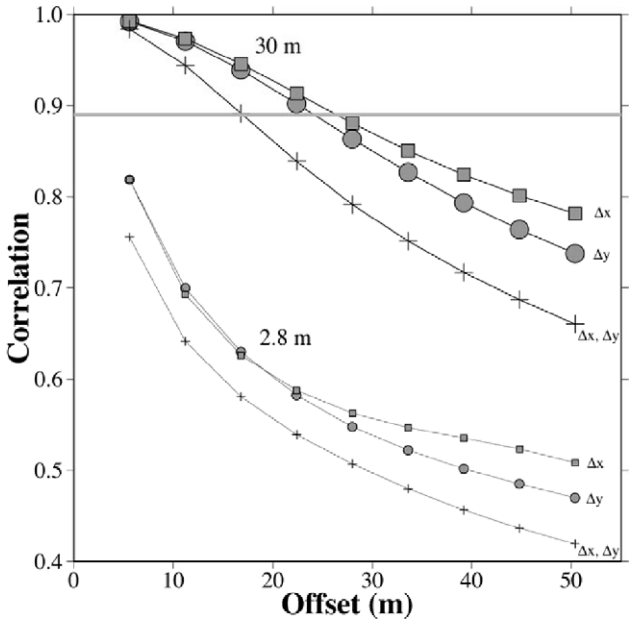

Fig. 9. Decorrelation of identical NYC vegetation fraction images with increasing offset. The smaller symbols show the decorrelation of the high resolution 2.8 m Quickbird vegetation fraction with eastward (Dx), northward (Dy) and diagonal (Dx, Dy) offsets. The larger symbols show the decorrelation when the high resolution fraction estimates are convolved with the Landsat ETM+ point spread function and resampled at 30 m resolution. The observed 0.89 correlation could be explained by a ~25 m lateral or a 17 m diagonal uncertainty in the position of the Landsat image—if the fraction estimates were in perfect agreement with the high resolution fractions.

Fig. 10. Simulated effect of spatial misregistration (Δx, Δy) and additive Gaussian error (s) on 30 m vegetation fraction correlation. Each scatterplot shows the correlation of identical 2.8 m vegetation fraction images subjected to spatial offset and convolved with the ETM+ point spread function. Gaussian error is added after convolution and resampling. Compare the scatter about the 1:1 diagonal with Fig. 9. The simulation indicates that the observed scatter is consistent with ~17 m spatial uncertainty and ~3% error. Error addition alone does not reproduce the scatter distribution.

abundance model (Ridd, 1995) for urban land cover—with one critical distinction. The SVD model represents biophysical surface reflectance properties while the VIS model represents biophysical land cover classes. The distinction is important because the SVD model represents features that can be distinguished from surface reflectance while the VIS model represents features that cannot necessarily be distinguished on the basis of reflectance alone.

Using broadband reflectance data to represent the V–I–S model is problematic because there is a fundamental ambiguity between the Impervious and Soil reflectances. As acknowledged in Ridd's original paper (Ridd, 1995), impervious surfaces often cannot be determined unambiguously in reflectance data. This is because impervious substrates do not have unique optical properties. In fact, many impervious surfaces (e.g. concrete and cement) are compositionally equivalent to pervious surfaces (e.g. carbonate mud and sand). Classifying pixels with high substrate fractions as impervious may provide reasonable approximations of actual impervious surface distribution in developed land areas in temperate and

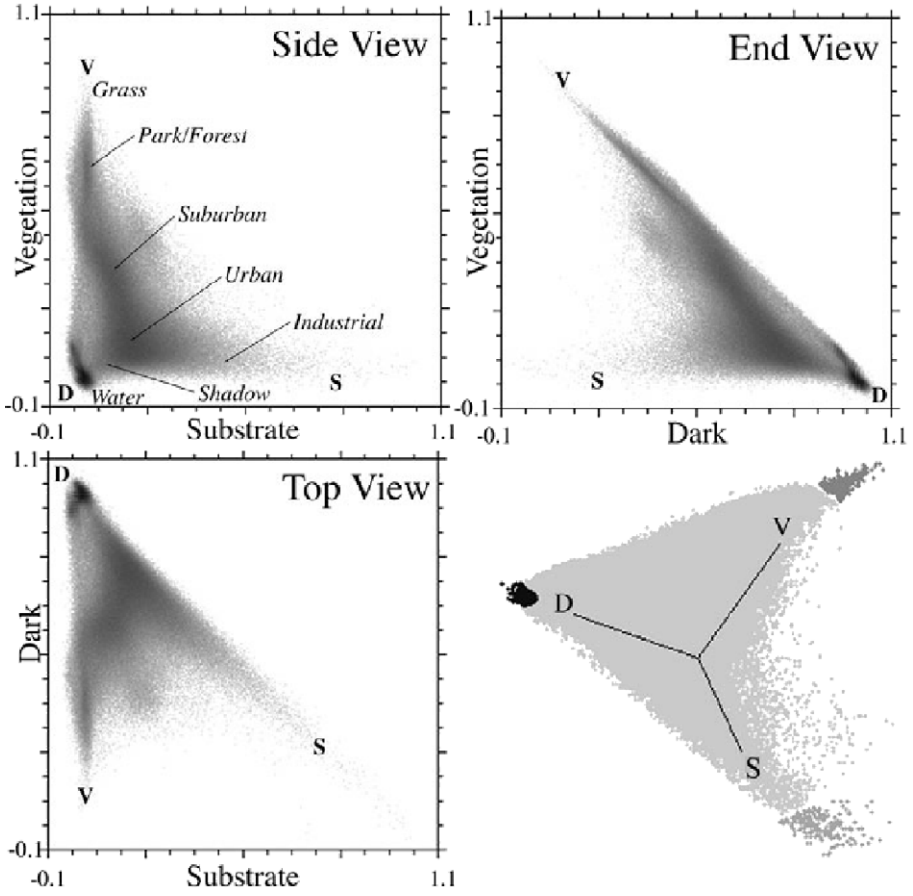

Fig. 11. Endmember fraction space. Density shaded scatterplots show orthogonal projections of the planar triangular feature space of endmember fractions. The side view illustrates the independence of the Vegetation and Substrate endmembers while the end and top views illustrate the reduction of each with increasing Dark fraction. In the side view the dark band trending from the vegetation endmember to the gray axis shows the progression from more to less vegetated land cover types. The oblique perspective (lower right) shows a view perpendicular to the planar cloud of pixels.

tropical climates where pervious surfaces often tend to be vegetated and exposed substrate tends to be impervious. However, the ambiguity can result in overestimates of impervious surface in areas where both pervious and impervious substrates are exposed and illuminated. This is a potentially serious problem in arid and semiarid climates because broadband sensors cannot generally distinguish between pervious and impervious surfaces on the basis of reflectance alone.

We propose here that vegetation fraction could provide constraints on the amount and spatial distribution of pervious surface thereby avoiding the assumptions inherent in reflectance-based estimates of impervious surface. If moderate resolution surface permeability constraints are needed for physical models a far more realistic strategy would be to use vegetation fraction as a proxy for fractional pervious surface rather than a binary classification of pervious and impervious. Treating vegetation fraction as a proxy for permeable surface distribution is admittedly ad hoc but it makes sense physically because vegetation cannot thrive on impervious surfaces so the presence of vegetation implies the presence of some amount of underlying permeable surface. In arid and semiarid climates, the presence of even low fractions of vegetation (above detection threshold) implies the presence of a somewhat permeable underlying surface. Although infiltration capacities of permeable surfaces can vary appreciably, using the presence of detectable vegetation as an indicator of permeable surface can account for a wide variety of natural and built landscapes. However, the fundamental ambiguity between permeable and impermeable substrates still exists on unvegetated (Fv < detection threshold) surfaces. While urban impervious surfaces can span a wide (and undiagnostic) range of reflectances on the gray axis, soil reflectance can often be more uniform at regional scales—provided moisture content is uniform. This may provide a way to distinguish unvegetated soils with consistent reflectance from a more diverse distribution of impervious surfaces in the urban mosaic.

5.2. Canopy shadow and illuminated vegetation

When using vegetation fraction estimates as inputs to physical models it is important to acknowledge the distinction between the area of illuminated vegetation and total quantity of vegetative matter. Vegetation fractions estimated from linear mixture models correspond to areal fraction of illuminated vegetation within the GIFOV—not vegetative biomass or leaf area index. This is illustrated with the vegetation fraction image of Central Park in New York shown in Fig. 12. At meter scales,

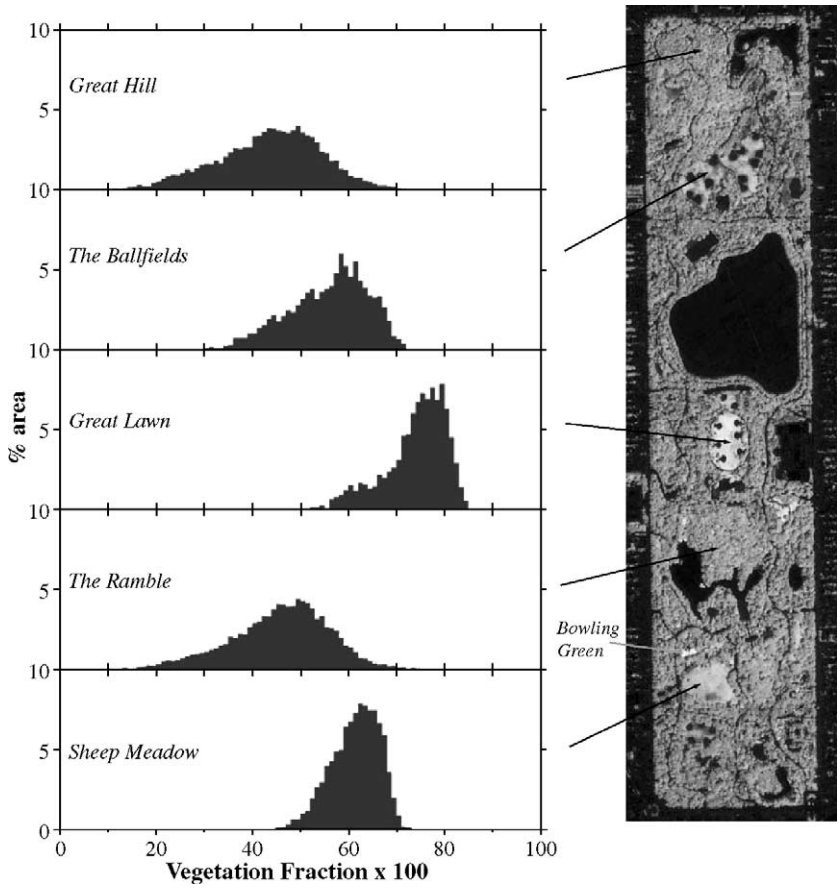

Fig. 12. Vegetation fraction distributions for closed canopy forest and grass in Central Park. Distributions of 2.8 m Quickbird vegetation fractions indicate the fraction of illuminated vegetation in typical forest canopy and varying density grass cover. 100% illuminated vegetation (fraction = 1.0) is calibrated to a well-maintained section of the Bowling Green. In comparison, typical grass cover is equivalent to 60% to 85% illuminated vegetation while closed canopy forest has median fractions in the 40% to 60% range.

trees are imaged as combinations of illuminated leaves and shadow with very small contributions from illuminated non-photosynthetic vegetation (stems, branches, etc.). The results from Central Park suggest that a typical deciduous tree crown will be imaged as pixels with illuminated vegetation fractions between 0.4 and 0.7 while the interstitial shadows between crowns have vegetation fractions between 0 and 0.4 depending on the depth of the shadow. At 30 m scales the canopy shadow mixes with illuminated crowns to yield aggregate fractions of 0.5 to 0.6. Unvegetated surfaces have vegetation fractions well under 0.2 at both scales. Poorly manicured grass shows considerable fractions of soil substrate endmember and typically has illuminated vegetation fractions between 0.4 and 0.9 depending on the health of the grass. In spite of this complication, high resolution fractions are considerably more informative than their moderate resolution equivalents because the diversity of possible distinct mixtures is considerably reduced by the finer spatial scale of the pixel. In other words many more spatial combinations of soil, shade and illuminated vegetation are possible within a 900 m^2 than within a 7.8 m^2 GIFOV, partly because the smaller GIFOV approaches the sizes of specific targets, such as a single tree. In terms of mapping vegetation abundance and distribution in urban areas, the bottom line is that Quickbird pixels are small enough to resolve many of the individual components that comprise the vast majority of the urban vegetation mosaic. Many physical process models represent vegetation with volumetric or biomass parameters. If consistent relationships between illuminated area and volume or biomass can be established and quantified then it may be possible to convert illuminated fraction to these parameters. Illuminated canopy fraction could also be a valuable quantity for photosynthesis-based models because it represents the fractional distribution of illuminated leaves that are directly receiving the most solar energy thereby influencing photosynthetic activity, transpiration and heat flux.

5.3. Applications to urban landscape management

Vegetation fractions derived from Landsat can be used to supplement the New York City Parks Department's street tree census and other unit-based inventories of vegetation resources. The census was first conducted in 1995–1996, and is planned to be done at 10 year intervals. The census itemized street trees by species, size, location and condition. It is extremely labor intensive, taking 13 months to complete with over 700 volunteers and Park staffs. Fig. 13 compares the mean vegetation fraction percentage in 2002 to the density of street trees counted in 1996 in each U.S. census tract, for each

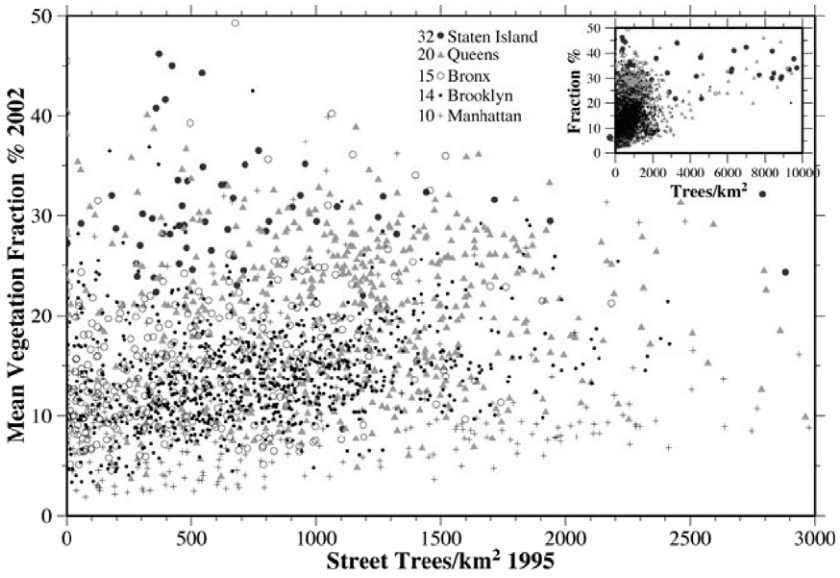

Fig. 13. Mean vegetation fraction versus street tree density for 2216 census blocks in the five boroughs of New York City. Minimum mean vegetation fraction increases with street tree density overall but there is considerable interborough variability in blocks with fewer street trees. This is expected as the street tree census does not count trees on private property and other types of vegetation. The variations among the boroughs correspond to differences in lot size and types of residential and commercial land use. Mean fractions for each borough are shown to the left of the symbols.

borough in New York City. The plot excludes park areas, for which no tree inventory exists. Street trees are just one aspect of all vegetation in New York City, whereas vegetation fraction measures all types of illuminated vegetation in a given area. As a result, there is no direct correspondence between mean vegetation fraction percentages and the density of street trees. The plot shows clear differences between boroughs for the relationship of mean vegetation fraction to the density of street trees, which reflects the different patterns of urban development between boroughs. For example, areas in Manhattan with a given density of street trees has a much lower mean vegetation fraction value than an area with the same density of street trees in Staten Island. Manhattan is dominated by tightly clustered tall buildings, causing shadowing which would lower the estimated vegetation fraction in an area. Staten Island is a borough that is suburban in character, with low detached housing and buildings surrounded by lawns and gardens, which is more amenable to measurement of vegetation from space. Consequently, Staten Island has higher vegetation fractions than areas in Manhattan with similar street tree densities. Similarly, Queens and the Bronx are boroughs with mixes of suburban and densely urban neighborhoods, whereas Brooklyn is a primarily urban borough but unlike Manhattan the pattern of development has resulted in mostly low buildings. In general, the variability between the boroughs reflects differences in the mix of land use types and the ratio of urban infrastructure to green space. Comparisons to public data such as the street tree census permits a rapid assessment of the proportion of an area's green resource that is comprised of publicly managed assets, potentially useful information for policy makers and government managers to use in planning.

Moderate resolution vegetation fraction estimates can provide a valuable tool for urban and suburban forestry. Most immediately, decision makers for urban areas can use Landsat TM and ETM+ vegetation fraction estimates to rapidly assess the state and distribution of urban vegetation across jurisdictional boundaries, a valuable tool for land-use planning and policy-making. While tree-by-tree inventories are useful for daily maintenance and situation specific decision making (like isolating blight and infestation) they are often limited by jurisdictional boundaries, prohibiting landscape/ecosystem scale management. From the perspective of environmental management urban vegetation performs many functions that improve urban quality of life. However, in situ mapping and monitoring of urban vegetation at regular intervals can be prohibitively expensive. We advocate a combined approach to vegetation monitoring in which remotely sensed vegetation fraction estimates are used as a periodic reconnaissance tool to focus in situ efforts and assets.

Effective monitoring of the health and distribution of urban vegetation can provide a number of benefits to urban residents. Trees provide habitat for urban wildlife and curb storm water runoff (Luley, 1998). Vegetation can also serve as sinks for carbon dioxide, and play a significant role in environmental quality and human health. Some estimates indicate that trees may absorb over 30% of urban and industrial air pollution, including carbon dioxide, ozone, and sulfur (Nowak et al., 2002; Luley, 1998). The presence of trees on an urban block can also reduce building energy needs for cooling and heating and thus mitigate the 'heat island effect' through shading (Simpson, 2002) and increasing latent heat flux at the expense of sensible heat. Under certain circumstances a block with only 20 trees on it can have its ground temperature lowered an average of 2.5 °C and humidity increased 2% (Bach, 1972). The 30+ year archive of TM and ETM+ imagery permits historical mapping of the abundance and spatial distribution of urban vegetation, allowing natural resource managers to make informed decisions about maintenance, planting and preserva-

tion. Maps of urban vegetation also serve as inputs to climate, air quality and hydrologic models that can ultimately help decision maker leverage ecosystem services to plan for and create sustainable, livable cities.

Vegetation fraction estimates using Quickbird imagery also show potential as a reconnaissance tool for managers. As Fig. 12 shows, fraction values can be used to differentiate between closed canopy forest versus grass areas. These values could be used to draw boundaries representing different vegetation classes as management zones. Intermediate vegetation fraction values not belonging clearly to closed canopy or grass would identify transition zones between these cover types, which require different management actions depending on whether the goal is a closed canopy or an open space. As archives of Quickbird imagery continue to build, fractions could be used to measure the changes over time in the abundance and distribution of these vegetation types.

6. Conclusions

Urban reflectance can be accurately represented with a three component linear mixture model for both Landsat ETM+ and Quickbird imagery in a wide variety of cities worldwide. The strong linearity of the Substrate Vegetation Dark surface (SVD) mixture model provides consistent estimates of illuminated vegetation fraction that can be used to constrain physical process models that require biophysical inputs related to vegetation abundance. When Quickbird-derived 2.8 m estimates of vegetation fraction are integrated to 30 m scales and coregistered to Landsat-derived 30 m estimates the median estimate agrees with the integrated fractions to within 5% for fractions >0.2. The scatter in the relationship cannot be explained with estimate error alone but is consistent with a 3% to 6% estimation error combined with a 17 m subpixel registration ambiguity. The 3D endmember fraction space obtained from ETM+ imagery corresponds to a ternary distribution of reflectance properties corresponding to distinct biophysical surface types. The SVD model is a reflectance analog to Ridd's V–I–S land cover model but acknowledges the fact that permeable and impermeable surfaces cannot generally be distinguished on the basis of broadband reflectance alone. We therefore propose that vegetation fraction be used as a proxy for permeable surface distribution to avoid the common erroneous assumption that all nonvegetated surfaces along the gray axis are completely impermeable. Comparison of mean vegetation fractions to street tree counts in New York City shows a consistent relationship between minimum fraction and tree count. However, moderate and high resolution areal estimates of vegetation fraction provide complementary information because they image all illuminated vegetation, including that not counted by the in situ street tree census.

Acknowledgements

C.S. gratefully acknowledges the support of the Environmental Protection Agency STAR program, the USDA Forest Service and the NASA Socioeconomic Data and Applications Center (SEDAC). This work is supported by the U.S. Environmental Protection Agency's National Center for Environmental Research (NCER) STAR Program, under Grant R-828733. Disclaimer: Although the research described in this presentation has been funded in part by the U.S. Environmental Protection Agency, it has not been subjected to the Agency's required peer and policy review and therefore does not necessarily reflect the views of the Agency and no official endorsement should be inferred.

References

Adams, J. B., Sabol, D. E., Kapos, V., Filho, R. A., Roberts, D. A., Smith, M. O., et al. (1995). Classification of multispectral images based on fractions of endmembers: Application to land cover change in the Brazilian Amazon. *Remote Sensing of Environment*, *52*, 137–154.

Adams, J. B., Smith, M. O., & Gillespie, A. R. (1993). Imaging spectroscopy: Interpretation based on spectral mixture analysis. In C. M. Pieters, & P. Englert (Eds.), *Remote geochemical analysis: Elemental and mineralogical composition* (pp. 145–166). New York: Cambridge University Press.

Adams, J. B., Smith, M. O., & Johnson, P. E. (1986). Spectral mixture modeling; a new analysis of rock and soil types at the Viking Lander 1 site. *Journal of Geophysical Research*, *91*, 8098–8122.

Asner, G. P. (1998). Biophysical and biochemical sources of variability in canopy reflectance. *Remote Sensing of Environment*, *64*, 234–253.

Asner, G. P., & Lobell, D. B. (2000). A biogeophysical approach for automated SWIR unmixing of soils and vegetation. *Remote Sensing of Environment*, *74*, 99–112.

Bach, W. (1972). Urban climate, air pollution and planning. In T. Detwyler, & M. Marcus (Eds.), *Urbanization and environment* (pp. I407–I418). Belmont: Duxbury Press.

Boardman, J. W. (1993). Automating spectral unmixing of AVIRIS data using convex geometry concepts. In R. O. Green (Ed.), *Fourth airborne visible/infrared imaging spectrometer (AVIRIS) airborne geoscience workshop* (pp. 11–14). Pasadena, CA: Jet Propulsion Laboratory.

Boardman, J. W., & Kruse, F. A. (1994). Automated spectral analysis: A geologic example using AVIRIS data, north Grapevine mountains, Nevada. *Tenth thematic conference on geologic remote sensing* (pp. I407–I418). Ann Arbor, MI: Environmental Research Institute of Michigan.

Elmore, A. J., Mustard, J. F., Manning, S. J., & Lobell, D. B. (2000). Quantifying vegetation change in semiarid environments: Precision and accuracy of spectral mixture analysis and the normalized difference vegetation index. *Remote Sensing of Environment*, *73*, 87–102.

Gillespie, A. R., Smith, M. O., Adams, J. B., Willis, S. C., Fischer, A. F., & Sabol, D. E. (1990). Interpretation of residual images: Spectral mixture analysis of AVIRIS images, Owens Valley, California. *Proceedings of the 2nd airborne visible/infrared imaging spectrometer (AVIRIS) workshop* (pp. 243–270). Pasadena, CA: NASA Jet Propulsion Laboratory.

Johnson, P. E., Smith, M. O., Taylor-George, S., & Adams, J. B. (1983). A semiempirical method for analysis of the reflectance spectra for binary mineral mixtures. *Journal of Geophysical Research*, (88), 3557–3561.

Kressler, F., & Steinnocher, K. (1996). Change detection in urban areas using satellite images and spectral mixture analysis. *International Archives of Photogrammetry and Remote Sensing*, *XXXI*(Part B7), 379–383.

Luley, C. J. (1998). The greening of urban air. *Forum for Applied Research and Public Policy*, *13*, 33–35.

Markham, B. L. (1985). The Landsat sensors' spatial responses. *IEEE Transactions on Geoscience and Remote Sensing*, *GE-23*(6), 864–875.

Markham, B. L., & Barker, J. L. (1986). Landsat MSS and TM post-calibration dynamic range, exoatmospheric reflectance and at-satellite temperatures. *Eosat-Landsat Technical Notes* (pp. 3–5).

Markham, B. L., & Barker, J. L. (1987). Thematic mapper bandpass solar exoatmospheric irradiances. *International Journal of Remote Sensing*, *8*(3), 517–523.

Nowak, D. J., & Crane, D. E. (2002). Carbon storage and sequestration by urban trees in the USA. *Environmental Pollution*, *116*, 381–389.

Nowak, D. J., Crane, D. E., & Dwyer, J. F. (2002). Compensatory value of urban trees in the United States. *Journal of Arboriculture*, *28*(4), 194–199.

Pech, R. P., Davies, A. W., Lamacraft, R. R., & Graetz, R. D. (1986). Calibration of Landsat data for sparsely vegetated semi-arid rangelands. *International Journal of Remote Sensing*, *7*, 1729–1750.

Rashed, T., Weeks, J. R., Gadalla, M. S., & Hill, A. G. (2001). Revealing the anatomy of cities through spectral mixture analysis of multispectral satellite imagery: A case study of the greater Cairo region, Egypt. *Geocarto International*, *16*(4), 5–15.

Rashed, T., Weeks, J., Stow, D., & Fugate, D. (2002). Measuring temporal compositions of urban morphology through spectral mixture analysis: Toward a soft approach to change analysis in crowded cities. In C. Jurgens, & D. Maktav (Eds.), *Proceedings of the third international symposium of urban remote sensing* (pp. 512–527). Istanbul, Turkey: Istanbul Technical University.

Ridd, M. K. (1995). Exploring a V–I–S (Vegetation–Impervious Surface–Soil) model for urban ecosystem analysis through remote-sensing—Comparative anatomy for cities. *International Journal of Remote Sensing*, *16*(12), 2165–2185.

Roberts, D. A., Batista, G., Pereira, J., Waller, E., & Nelson, B. (1998a). Change identification using multitemporal spectral mixture analysis: Applications in eastern Amazonia. In C. Elvidge, & R. Lunetta (Eds.), *Remote sensing change detection: Environmental monitoring applications and methods* (pp. 137–161). Ann Arbor: Ann Arbor Press.

Roberts, D. A., Gardner, M., Church, R., Ustin, S., Scheer, G., & Green, R. O. (1998b). Mapping chapparal in the Santa Monica mountains using multiple endmember spectral mixture models. *Remote Sensing of Environment*, *65*, 267,179.

Sabol, D. E., Adams, J. B., & Smith, M. O. (1992). Quantitative sub-pixel spectral detection of targets in multispectral images. *Journal of Geophysical Research*, *97*, 2659–2672.

Settle, J. J., & Drake, N. A. (1993). Linear mixing and the estimation of ground cover proportions. *International Journal of Remote Sensing*, *14*(6), 1159–1177.

Simpson, J. R. (2002). Improved estimates of tree-shade effects on residential energy use. *Energy and Buildings*, *34*, 1067–1076.

Singer, R. B. (1981). Near-infrared spectral reflectance of mineral mixtures: Systematic combinations of pyroxenes, olivine and iron oxides. *Journal of Geophysical Research*, *86*, 7967–7982.

Singer, R. B., & McCord, T. B. (1979). Mars: Large scale mixing of bright and dark surface materials and implications for analysis of spectral reflectance. *10th Lunar and planetary science conference* (pp. 1835–1848). Rome, Italy: American Geophysical Union.

Small, C. (2001a). Estimation of urban vegetation abundance by spectral mixture analysis. *International Journal of Remote Sensing*, *22*(7), 1305–1334.

Small, C. (2001b). Multiresolution analysis of urban reflectance. In T. Bucciarelli, & O. Hellwich (Eds.), *IEEE/ISPRS conference on remote sensing of urban areas* (pp. 671–677). Rome, Italy: IEEE.

Small, C. (2002a). A global analysis of urban reflectance. In D. Maktav, F. Sunar-Erbek, & C. Jurgens (Eds.), *Proceedings of the third international symposium on remote sensing of urban areas*. Istanbul, Turkey.

Small, C. (2002b). Multitemporal analysis of urban reflectance. *Remote Sensing of Environment*, *81*(2–3), 427–442.

Small, C. (2003). High spatial resolution spectral mixture analysis of urban reflectance. *Remote Sensing of Environment*, *88*(1–2), 170–186.

Small, C. (2004). The Landsat ETM+ spectral mixing space. *Remote Sensing of Environment*, *93*, 1–17.

Small, C. (2005). A global analysis of urban reflectance. *International Journal of Remote Sensing*, *26*(4), 661–681.

Small, C., & Miller, R. B. (1999). Digital cities II: Monitoring the urban environment from space. *Proceedings of the international symposium on digital earth* (pp. 671–677). Beijing, China: Chinese Academy of Sciences.

Smith, M. O., Ustin, S. L., Adams, J. B., & Gillespie, A. R. (1990). Vegetation in deserts: I. A regional measure of abundance from multispectral images. *Remote Sensing of Environment*, *31*, 1–26.

Watt, F. S. (1998). The State of Our Street Trees: Report on the 1996 New York City Street Tree Census. City of New York, Parks and Recreation, unpublished report.

Weng, Q., Lu, D., & Schubring, J. (2004). Estimation of land surface temperature–vegetation abundance relationship for urban heat island studies. *Remote Sensing of Environment*, *89*, 467–483.

Wu, C., & Murray, A. T. (2003). Estimating impervious surface distribution by spectral mixture analysis. *Remote Sensing of Environment*, *84*, 493–505.